ELSEVIER

Journal of Atmospheric and Solar-Terrestrial Physics 68 (2006) 999–1017

Journal of ATMOSPHERIC AND SOLAR-TERRESTRIAL PHYSICS

www.elsevier.com/locate/jastp

Small-scale fluctuations and scintillations in high-resolution GPS/CHAMP SNR and phase data

Dong L. Wu*

Jet Propulsion Laboratory, California Institute of Technology, Pasadena, California, USA

Received 28 February 2005; received in revised form 23 August 2005; accepted 3 January 2006
Available online 21 April 2006

Abstract

This paper analyzes small-scale fluctuations that appear in the signal-to-noise ratio (SNR) and phase measurements during GPS/CHAMP radio occultation through the E-region ionosphere, lower stratosphere, and upper troposphere. Analyses are based on the raw 50-Hz SNR and phase data, which reveal new information on variations and distributions of small-scale atmospheric/ionospheric variabilities that would be normally discarded in the retrieved temperature profiles. The derived SNR and phase variances show strong annual and interannual variations in the ionosphere due to solar-cycle modulated sporadic-E activity. The intensity of polar E_s activity reduced gradually since 2001, as solar activity weakened from the 2000 maximum. In the upper troposphere, the small-scale SNR and phase variances maximize near the tropical tropopause and vary strongly with seasonal variations of the tropopause. In the tropical lower stratosphere, the variances exhibit a quasi-biannual oscillation (QBO) with amplitude maximized at altitudes of 15–30 km and progressing downward in time. The downward-progressing amplitude occurs just below the height of zero-wind line where QBO changes phase from the easterly to the westerly. Physical interpretation of SNR and phase variances is made with analytical expressions derived for idealized small-scale ionospheric and atmospheric perturbations. In these cases, the SNR standard deviation is inversely proportional to vertical wavelength of perturbations whereas the phase one is proportional to the truncation length used for variance calculations.

Keywords: Scintillation; Gravity wave; GPS radio occultation; Ionosphere; Troposphere

1. Introduction

In satellite-to-satellite radio communications, such as GPS-LEO (Global Positioning System–Low Earth Orbiter) radio occultation (RO), the receiver signal amplitude (SNR or signal-to-noise ratio) and phase measurements are often subject to strong scintillations from structured perturbations in the ionosphere and neutral atmosphere. High-rate (50 or 100 Hz) RO data provide unique observations on these ionospheric and atmospheric fine structures with unprecedented vertical resolution. Currently, these fine-scale phenomena are not well understood, and neither is the connection between raw RO measurements and ionospheric/atmospheric variabilities, despite a number of studies on perturbations by sporadic-E (E_s) and gravity waves (GWs) (e.g., Hocke et al., 2001; Ratnam et al., 2004; Randel and Wu, 2005). Most of these studies are

*Fax: +1 818 3935065.
E-mail address: dwu@mls.jpl.nasa.gov.

1364-6826/$ - see front matter © 2006 Elsevier Ltd. All rights reserved.
doi:10.1016/j.jastp.2006.01.006

based on the retrieved products, such as total electron content (TEC), temperature, and water vapor, in which vertical resolution has been reduced. Thus, higher-frequency (>1 Hz) oscillations in the SNR (SNR amplitude) and phase data are not fully utilized. Instead, some of the high-frequency fluctuations are treated as noise and smoothed out before the retrievals. This "noise", however, contains valuable information on small-scale structures in the ionosphere and in the lower atmosphere (Marquardt and Healy, 2005).

Several studies made direct use of the high-resolution SNR and phase data (e.g., Igarashi et al., 2002; Pavelyev et al., 2003; Gavrilov et al., 2004; Wu et al., 2005), but much work is needed to understand the nature of the scintillation problem. GPS occultation is operated at two L-band frequencies: L1 = 1.6 GHz and L2 = 1.2 GHz, between LEO receivers and GPS transmitters. The raw SNR and phase data have several advantages for studying small-scale features. First, small-scale information is best preserved in the raw L1 data. The temperature and water vapor retrievals rely on the noisier L2 data and information about GPS orbits and clocks, where additional noise can be introduced. Second, retrieval processes (e.g., the Abel inversion) assume spherical symmetry, which is usually not a valid assumption in the presence of small-scale disturbances. Perturbations in the retrieved variables become difficult to interpret in these cases (Hajj and Romans, 1998). Corrections to the retrieved quantities can be made if the observed structures are known (e.g., stratospheric GWs as described in Lange and Jacobi, 2003). Third, measurement noise in the raw data is relatively simple to characterize and analyze. Finally, more RO profiles can be used because quality control is less strict than in the normal retrievals. For example, to study ionospheric perturbations, one can extract phase perturbations at high tangent heights without requiring good accuracy on L1 and L2 phase measurements.

This study extends the E_s analysis by Wu et al. (2005) with SNR and phase measurements to further investigate wave activity in the lower atmosphere. The 50-Hz GPS/CHAMP data are used to produce climatology of SNR and phase fluctuations as a function of time and altitude. The observed variations of phase variances show a strong dependence on the cut-off wavelength used, and analytical expressions are derived from some idealized cases to interpret the observed variance properties in relation to wave amplitude and vertical wavelength.

2. Data analysis

The GPS constellation consists of about 30 satellites (canonically 24 plus a few spares) that are distributed roughly in six circular orbital planes with $\sim 55^\circ$ inclination at 20,200-km altitude (Spilker, 1980). Precise measurements of time delay between GPS transmitters and LEO receivers are used to obtain profiles of atmospheric pressure, temperature, and water vapor (e.g., Kursinski et al., 1997) or electron density (Hajj and Romans, 1998). These profiles have excellent vertical resolution that is not readily achieved by other satellite remote sensing techniques. Remote sensing of Earth's atmosphere with the GPS occultation technique was first demonstrated in GPS/MET (GPS meteorology) mission during 1995–1997 (Ware et al., 1996). The recent missions, such as the German Challenging Mini-satellite Payload (CHAMP) (Wickert et al., 2001), the Argentinean SAC-C (Satelite de Aplicaciones Cientificas-C) (Hajj et al., 2004), and the DoD Ionospheric Experiment (IOX) (Straus et al., 2003) are producing a total of $\sim$600 occultations per day. Future GPS occultation missions, such as COSMIC (Constellation Observing System for Meteorology, Ionosphere, and Climate) and C/NOFS (Communications/Navigation Outage Forecasting System), will provide over 3000 profiles per day with dense geographical and local time coverage.

The CHAMP satellite acquires 200–250 occultations per day but the number of profiles in the Level 2 data (Reigber et al., 2002) is significantly less (by $\sim$20%) due to strict quality control for temperature and water vapor retrievals. CHAMP sampling is sparse, not enough to make daily maps, but can produce useful monthly and seasonal statistics. CHAMP orbit precesses in local time at a rate of $\sim$5.6 min/day at the equator, covering a complete 24-h cycle every $\sim$130 days with both ascending and descending orbits. However, the actual revisiting period is shorter ($\sim$108 days) because the CHAMP receiver has a broad antenna field of view ($\sim 70^\circ$) and can make occultation from GPS satellites within ± 1 h from its suborbital local time.

2.1. Atmospheric and ionospheric effects

The atmosphere/ionosphere interacts with radio wave propagation through atmospheric refractivity, $N = (n-1) \times 10^6$, where n is the index of refraction. At the L1 and L2 frequencies, refractivity

depends primarily on atmospheric temperature T, total and water vapor pressure (P and P_{wv}), electron density n_e, and radio frequency f, i.e.,

$$N = 77.6\,\frac{P}{T} + 3.73\times 10^5\,\frac{P_{wv}}{T^2} - 4.03\times 10^7\,\frac{n_e}{f^2}, \quad (1)$$

where P and P_{wv} are in h Pa, T is in K, n_e is in m^{-3}, and f is in Hz. Other minor effects on the refractivity can be neglected and effects of small perturbations due to atmospheric/ionospheric structures are discussed in Appendix A. For GPS RO measurements, the most important atmospheric/ionospheric effects are summarized in Hajj et al. (2002) including: (1) dending effect on phase delay, (2) defocusing/focusing effect on SNR, (3) diffraction effect, and (4) multipath effect.

2.2. SNR and phase fluctuations

GPS-LEO RO often experiences strong scintillations in the SNR and phase measurements at the L1 and L2 frequencies. These scintillations can be well measured with the 50 Hz or 100 Hz sampling to yield important clues about their cause(s). Fig. 1 shows an example of the CHAMP 50-Hz L1 SNR and phase measurements taken in January 2002. This occultation descends from the upper atmosphere at a rate of ~2.2 km/s. The SNR before affected by the neutral atmosphere is close to ~800, hereafter referred as to SNR_0. The L1 phase delay varies with tangent height at a slow rate above ~40 km, which is attributed mainly to the ionospheric delay. The phase delay starts to increase exponentially below ~40 km as the bending from the neutral atmosphere takes effect. The atmospheric component of the phase delay, called iono-free phase delay ($\phi_{\text{iono-free}}$), can be derived using simultaneous L1 and L2 phase measurements (ϕ_1 and ϕ_2, respectively), i.e.,

$$\phi_{\text{iono-free}} = 2.5457\phi_1 - 1.5457\phi_2. \quad (2)$$

As shown in Fig. 1, the SNR/SNR_0 fluctuates largely at tangent heights above ~50 km due to electron density irregularities in the sporadic-E (E_s). Similarly, the L1 phase fluctuates at the same tangent heights showing good correlation with the

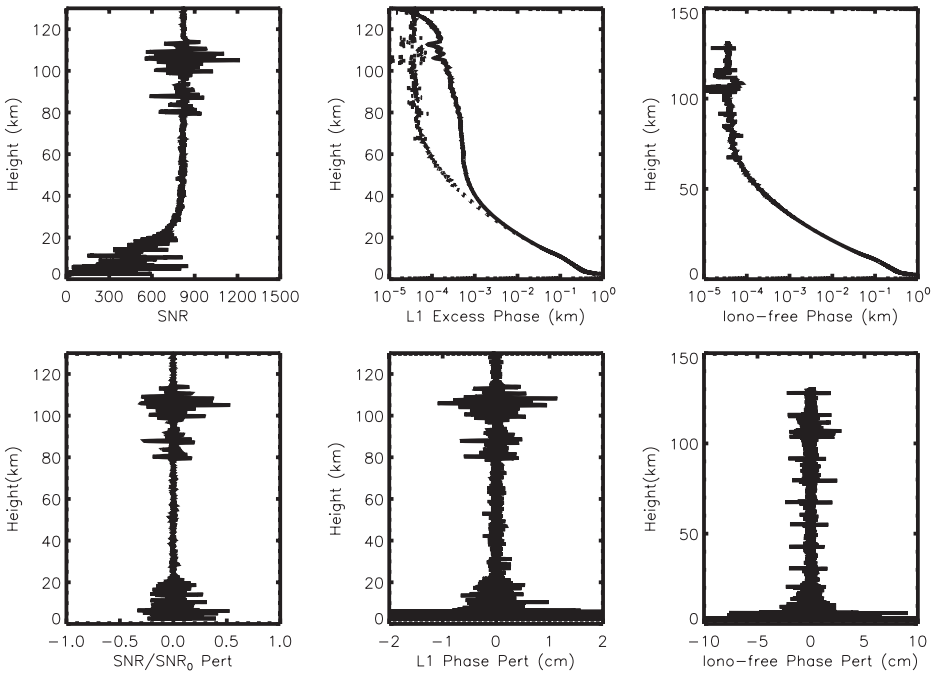

Fig. 1. An example of GPS/CHAMP occultation at 50.5S and 163.9W on January11, 2002. The top row shows 50 Hz measurements of SNR, L1, and iono-free phases. The iono-free phase profile is duplicated in the L1 phase panel as the dotted line to highlight the atmospheric and ionospheric contributions. The bottom row shows perturbations of the SNR and the phases extracted with a 2-s high-pass filter, where the SNR perturbations are normalized to its free-space average. The same high-pass filter is applied twice to the phase measurements in order to detrend the exponentially varying data. The periodic spikes in iono-free phase perturbations come from L2 phase, which is associated mainly with the receiver hardware.

SNR/SNR_0 events. Due to larger noise in the L2 signal, the iono-free data provide little information on the natural atmosphere above 35 km.

In addition, ionospheric fluctuations are not completely removed in the derived iono-free phase. The incomplete removal, as shown in Wu et al. (2005), is partly caused by the lag between the L1 and L2 phase fluctuations that are sometimes associated with thin-layer structures. Other mechanisms, such as different ray paths associated with the two frequencies, can also cause the residual oscillations from the E-region ionosphere. A correction based on higher order f dependence and precise bending angles is needed to completely remove ionospheric effects.

In Fig. 1, part of the SNR and phase oscillations is due to instrument/measurement noise, which contains random and systematic components. The L2 measurements are generally noisier than L1 due to weaker SNR. As a result, the iono-free phase is largely limited by the L2 measurement error in $\sigma^2_{\phi_{\text{iono-free}}} = 2.5457^2\sigma^2_{\phi 1} + 1.5457^2\sigma^2_{\phi 2}$. Therefore, above 35 km, the iono-free phase error is determined primarily by the L2 error and the ionospheric residual.

2.3. Variance analysis

To extract small-scale SNR and phase perturbations, we first detrend occultation profiles with an N-point high-pass filter, which is the difference between measurement and smoothed profile from the N-point running windows. Since the phase measurements vary exponentially with height, in addition to this high-pass filter, a third-order polynomial filter is applied to make a steeper truncation for long wavelengths. An example of the 51-point high-pass filter is shown in Fig. 2 for the SNR and phase measurements.

The detrended data, as shown in the bottom panel of Fig. 1, contain the SNR perturbations (normalized by SNR_0) and phase perturbations for L1 and iono-free measurements. Large oscillations due to E_s are clearly evident in the SNR/SNR_0 and phase perturbations at tangent heights of 80–120 km. The SNR shows perturbations as high as 50% while L1 phase exhibits a peak-to-peak amplitude of 10 cm. Both SNR and phase fluctuations due to E_s reduce substantially at tangent heights below 80 km, which is approximately the bottom of the ionosphere. It does not disappear

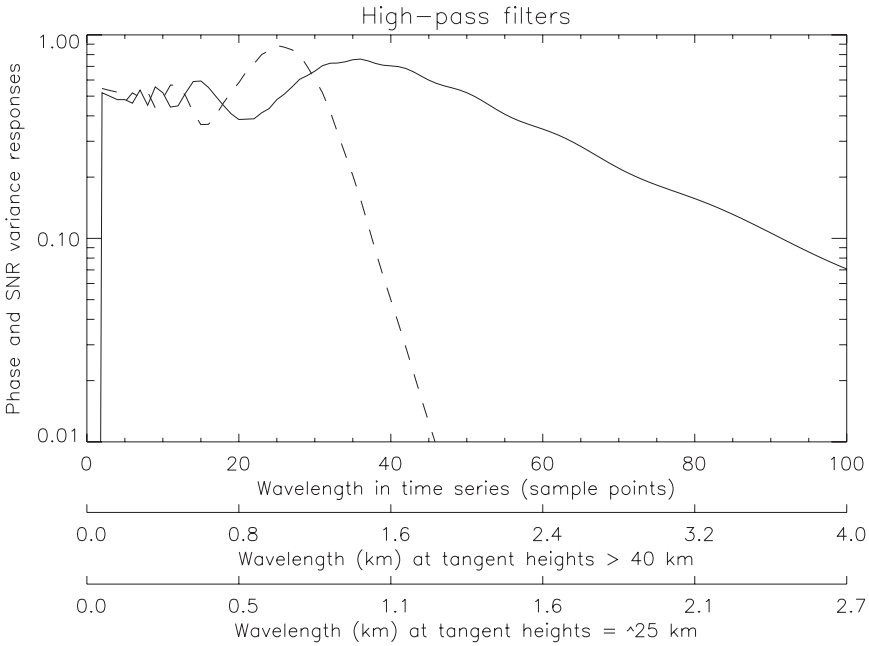

Fig. 2. High-pass filters for SNR (solid) and phase (dashed) using a 50-point truncation. Based on the CHAMP RO descending speed, estimated vertical scales are labeled below the number of sample points, and this conversion depends on tangent heights. At tangent heights >40 km, bending is small and the descending speed is ~2 km. As bending increases at 25 km, the descending speed decreases by 50%.

completely because the occultation ray still passes through the ionosphere with a slant angle. As shown in Wu et al. (2005), fluctuations maximize when the ray is parallel to E_s layers and decrease sharply in amplitude when it deviates from the parallelism. At tangent heights below ~40 km, fluctuations are dominated by neutral atmospheric variabilities caused by dry air and water vapor density fluctuations.

To remove high-frequency spikes in the phase measurements (seen in the iono-free phase perturbations), we apply a 3-point filter in addition to the N-point filter to form a (N, 3) band-pass filter where most noise power at frequencies greater than 10 Hz can be effectively removed. Similar to the method used in Wu et al. (2005), we processed the 50-Hz CHAMP data with several band-pass filters: (801,3), (601,3), (401, 3), (201, 3), (101, 3), (51, 3), and (21, 3), and averaged the variances on a monthly basis. The 401-point truncation corresponds to vertical wavelength truncations of ~16 km in the ionosphere, but reduces to ~10, ~6, and ~3.5 km at 25, 15, and 8 km altitudes, respectively.

The SNR and phase variances, σ^2, can be written as a sum of several sources:

$$\sigma^2 = \sigma_A^2 + \sigma_{E_s}^2 + \sigma_F^2 + \sigma_\varepsilon^2, \quad (3)$$

where $\sigma_A{}^2$, $\sigma_{E_s}^2$, σ_F^2, and σ_ε^2 are, respectively, associated with the neutral atmosphere, E_s, F-ionosphere, and instrument noise. The instrument noise, including radiometric and clock errors, can be non-random and non-stationary. Because these instrument errors vary from occultation to occultation, we must remove them on a profile-by-profile basis. The F-region fluctuations normally generate very noisy measurements over a broad range of tangent heights (Straus et al., 2003), extending far above and below 100 km. We removed most of the F-region scintillations by discarding profiles if the averaged 3-point variance is 100 times greater than its monthly mean at tangent heights >120 km or between 40 and 80 km. The number of monthly RO profiles useful for tropospheric sounding is typically $\sim 1.2 \times 10^5$ and the number of the rejected profiles is <0.05%.

Fig. 3 shows the SNR and phase variances derived from CHAMP RO using the (201, 3) filter. The SNR variance is normalized by its free-space value SNR_0, which becomes similar to S_4 index used in ground-based observations (Yeh and Liu, 1982). The E_s-related variances peak in the summer mid-latitudes at ~105 km. E_s effects on the variance are extended to tangent heights as low as ~40 km, which can be identified as a coherent variation with its structure at 105 km. In the lower atmosphere, large variances are found slightly above the tropopause and below 10 km, similar to the distribution found with GPS/MET data (Gavrilov et al., 2004). Because waves from the lower atmosphere can propagate and grow in amplitude with height, neutral atmospheric variabilities can become significant by overcoming the measurement noise or ionospheric residuals at high altitudes. Thus, at heights >~40 km, the L1 SNR and phase variances are mixed with atmospheric and ionospheric components. In the worst case (e.g., polar regions with high solar activity), ionospheric fluctuations can affect the SNR and phase variances at ~25 km tangent heights. In the normal condition, the lowest E_s variance occurs at the latitude band of 30°S–40°S and at tangent heights of 35–70 km in January.

The iono-free phase variance would be the best measurement to study the neutral atmospheric component at higher altitudes if the measurement noise were not degraded severely by the L2 data. However, as shown in Fig. 1, the iono-free data have much larger noise than the L1 phase at heights above ~25 km (mainly due to the noisy L2 measurement). Therefore, the iono-free data suffer substantially from the L2 noise and could not observe the atmospheric variances at many altitudes of interest. In addition, E_s effects cannot be completely removed in the iono-free phase measurements at high altitudes, as illustrated Fig. 1, where E_s features remain considerably above the noise level at 60–120 km. The possible cause of this E_s residual has been discussed previously (Wu et al., 2005), which was thought due to temporal lags between L1 and L2 measurements when the occultation scans through some thin E_s layers. E_s irregularities can affect phase variances at lower tangent heights as occultation paths intersect with E_s layers off the tangent point (Wickert et al., 2004), but the variance decreases substantially as tangent height lowers.

3. Sporadic-E (E_s) layers

E_s layers usually form irregularly in a narrow altitude region in the E-region ionosphere. Observations of E_s were mostly from ground-based remote sensing in the past decades, sometimes with in situ techniques (e.g., Whitehead, 1989; Mathews, 1998; Fukao et al., 1998). Only recently, GPS RO

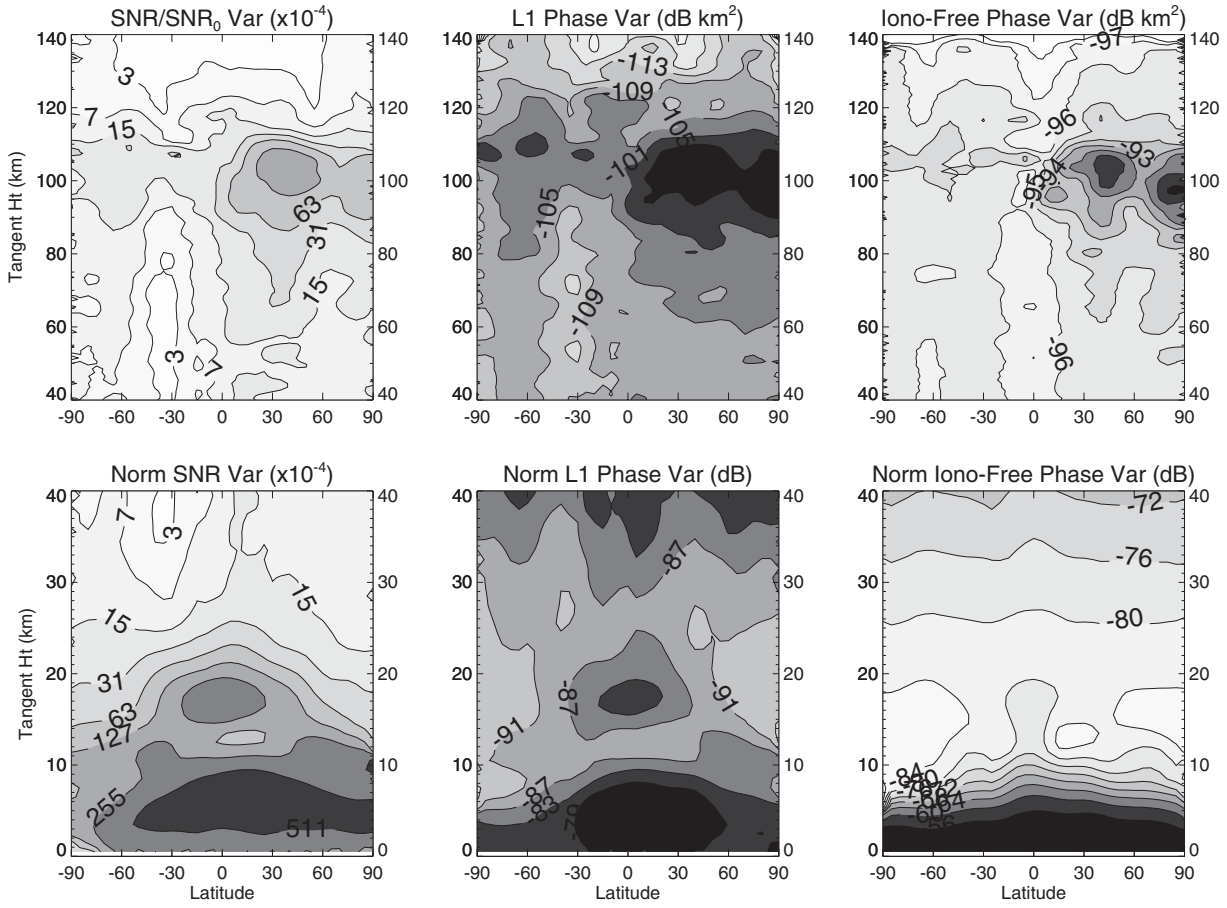

Fig. 3. Monthly mean SNR and phase variances for August 2004 using the (201,3) band-pass filter. Above ~50 km, the variances are dominated by E_s variability whereas the neutral atmospheric variability is mostly responsible to the variance at heights below 30 km. There are some mixed contributions at heights in between. In the lower atmosphere, the SNR and phase variances are normalized by their mean profiles at each latitude bin so as to highlight the neutral atmospheric component. The phase variances are either in dB km^2 or in dB, depending on whether they are normalized.

measurements are used to study such phenomena (Hocke et al., 2001; Pavelyev et al., 2003; Wickert et al., 2004; Liou et al., 2005; Wu et al., 2005; and references therein). By analyzing the CHAMP SNR and phase data, Wu et al. (2005) showed that global E_s activity enhances in the summer hemisphere with the maxima at ~105 km near 45°S in January 2003 and ~102 km near 45°N in June 2002. E_s seasonal variations are height-dependent, showing the peaking time delayed with altitude during northern summers.

The E_s activity distribution at 105 km was found to have a strong dependence on the geomagnetic dip angle I. The summertime mid-latitude E_s occurs mostly at $|I| = 30$–$60°$ while the wintertime polar E_s occurs at $|I| > 80°$. A significant semidiurnal variation was observed in the mid-latitude E_s variances with peak hours around 8:00–10:00 and 20:00 in local time at 100 km during June–August. During December–February, the summertime E_s is dominated by a diurnal variation with the peak hour near 20:00 in local time.

Fig. 4 shows the time series of CHAMP SNR and phase variances at 60–120 km altitudes where E_s induces most of small-scale RO fluctuations. A strong annual variation is evident at these altitudes in all latitude bands. Enhanced activity is found at summer mid-latitudes and repeats annually with peak amplitudes at ~110 km. A quasi-biannual oscillation (QBO)-like modulation is also evident with the SNR and phase variances at 70–110 km, showing higher amplitudes in 2003 and 2005

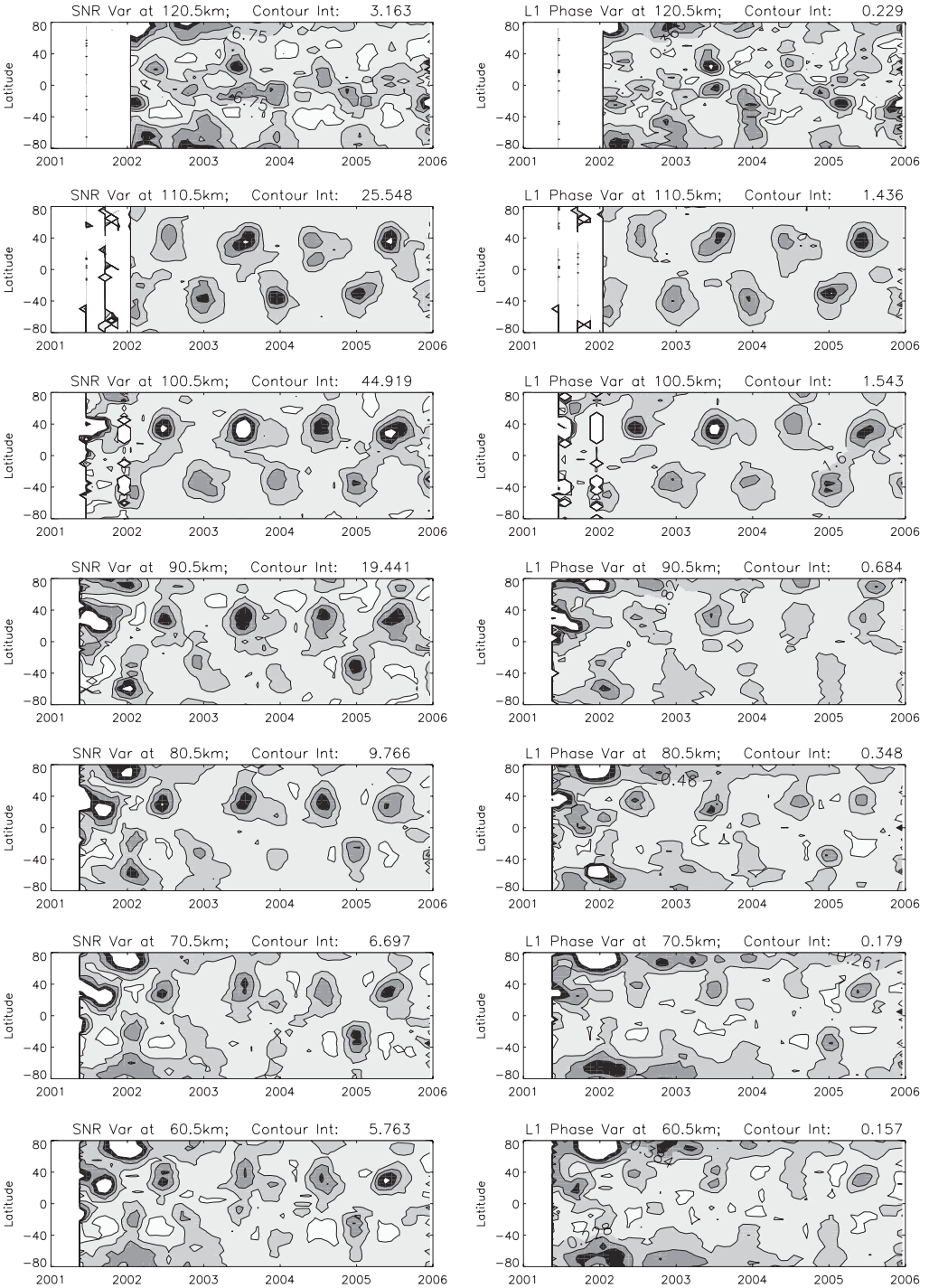

Fig. 4. Time series of SNR and phase variances during 2001–2004 at 60–120 km. The (201,3) filter is used for the variance calculations. The units for SNR/SNR_0 and L1 phase variances are 10^{-4} and m^2, respectively, and the contour intervals are indicated at the top of each panel. Data above 100 km were not available during the early period of CHAMP mission, and the missing period is indicated by white strips.

northern summers in the Northern Hemisphere (NH). In the Southern Hemisphere (SH), higher amplitudes are seen at 80–90 km in southern summers in 2002–2003 and 2004–2005. The mid-latitude variance nearly diminishes at heights <70 km in the SH whereas one at NH mid-latitudes remains significant. Therefore, the NH E_s variance, although occurring around $\sim$110 km, can affect the SNR and phase measurements at much lower tangent heights but shifts slightly toward the equator as height decreases. Compared to mid-latitude E_s, the high-latitude E_s activity has deeper impacts on variances at lower altitudes (Wickert et al., 2004). The high-latitude activity appears to maximize during October–January in both hemispheres with a decreasing trend since 2001. This correlates well with the 11-year solar cycle which has a maximum in 2000. The solar activity is known having large impacts on E_s activity (Maksyutin et al., 2001). In November 2001, some widespread Aurora Borealis and geomagnetic storms were observed over many parts of the NH.

4. Fluctuations in the lower atmosphere

The most prominent features of the SNR and phase variances in the lower atmosphere are associated with the tropopause. The tropopause is a transition layer separating the convectively controlled troposphere from the radiatively controlled stratosphere. Hence, both convective processes and large-scale residual circulation are important in determining the tropopause structure and variability. By heating the troposphere, cumulus convection weakens its stability and results in an elevated and cooler tropopause. In addition, the residual circulation in the stratosphere drives a slow mean upwelling motion, which can also raise the tropopause height and reduces its temperature through adiabatic cooling.

With the raw SNR and phase data, one of the greatest challenge is to separate between those induced by ionospheres and those by the neutral atmosphere. Because RO in the lower atmosphere always passes through the ionosphere, phenomena like E_s can contaminate the observations at lower altitudes. Nevertheless, as shown in Wu et al. (2005), the E_s-induced variance maximizes at the height where layers are formed, and reduces significantly in amplitude as tangent height is lowered. To minimize the potential ionospheric influence, we exclude the profiles if the variance at 40–80 km is exceptionally larger ($100\times$) than the average.

4.1. Tropopause variabilities

The SNR and phase variances correlate well with the tropopause height. Tropopause height and temperature can change by as much as 1 km and 6 K in the tropics from season to season (Reid and Gage, 1981; Salby and Callaghan, 2004; Schmidt et al., 2004a). The tropopause is highest and coldest during northern winter, when deep convection is highest and coldest, and centered near the equator. As shown in Fig. 5, the 18.5 km variance maximizes in northern winters whereas the 16.5 km variance maximizes in northern summers when the tropopause is lower. The latitudinal variations of CHAMP variances in the tropics and subtropics are similar to the observations from GPS/MET at 16–22 km (Tsuda et al., 2000). As the tropopause moves down at mid-latitudes, so does the variance maxima. The variances at 14.5 and 10.5 km reflect the tropopause variations at mid- and high latitudes, respectively. The 10.5 km variances indicate strong polar variations in northern summers while only moderate seasonal and annual modulations are observed in SH high latitudes.

The atmospheric component of the SNR and phase variances decreases with height at altitudes $>\sim$25 km and is overwhelmed by ionospheric contributions. During northern winters, ionospheric effects on the variance at low tangent heights become serious at high latitudes where ionospheric contributions can extend to tangent heights as low as 25 km. At 25–45 km, the ionospheric contributions are relatively weak at lower latitudes such that neutral atmospheric variability can be readily observed. As discussed in the following, the most prominent features of neutral atmospheric variabilities are the annual variation and QBO in the subtropical and tropical regions.

4.2. Lower stratospheric variances

To verify atmospheric components in the SNR and phase variances, one can compare them with the iono-free phase measurement. For example, at 25 km, the iono-free variance is only valid for two long-wavelength filters (Fig. 6), i.e., (401, 3) and (601, 3), because atmospheric variances are too weak to observe with short-wavelength cutoffs. For the two comparable variances, the regions with

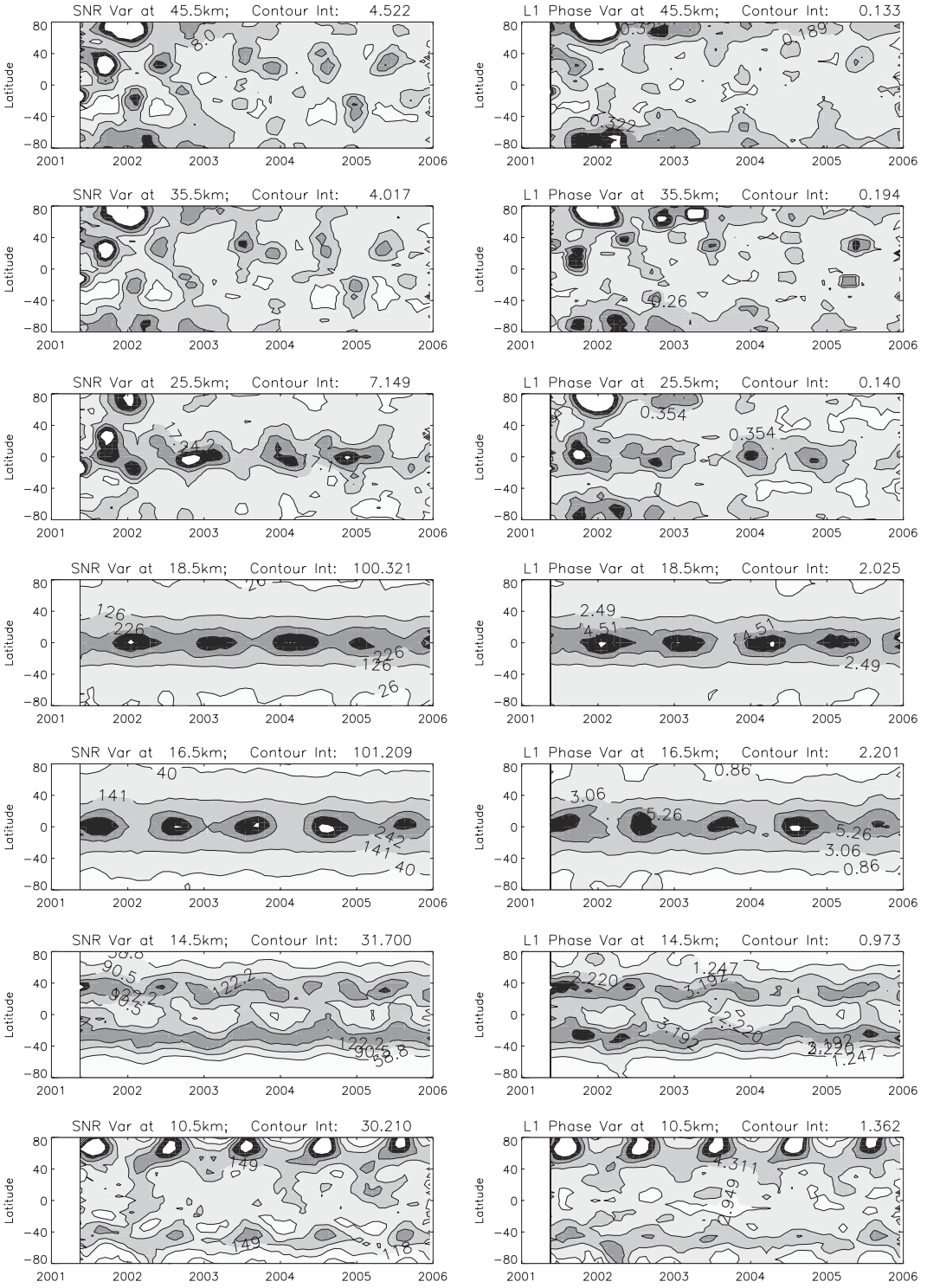

Fig. 5. Similar to Fig. 4 except that it is for seven altitudes at 10–45 km.

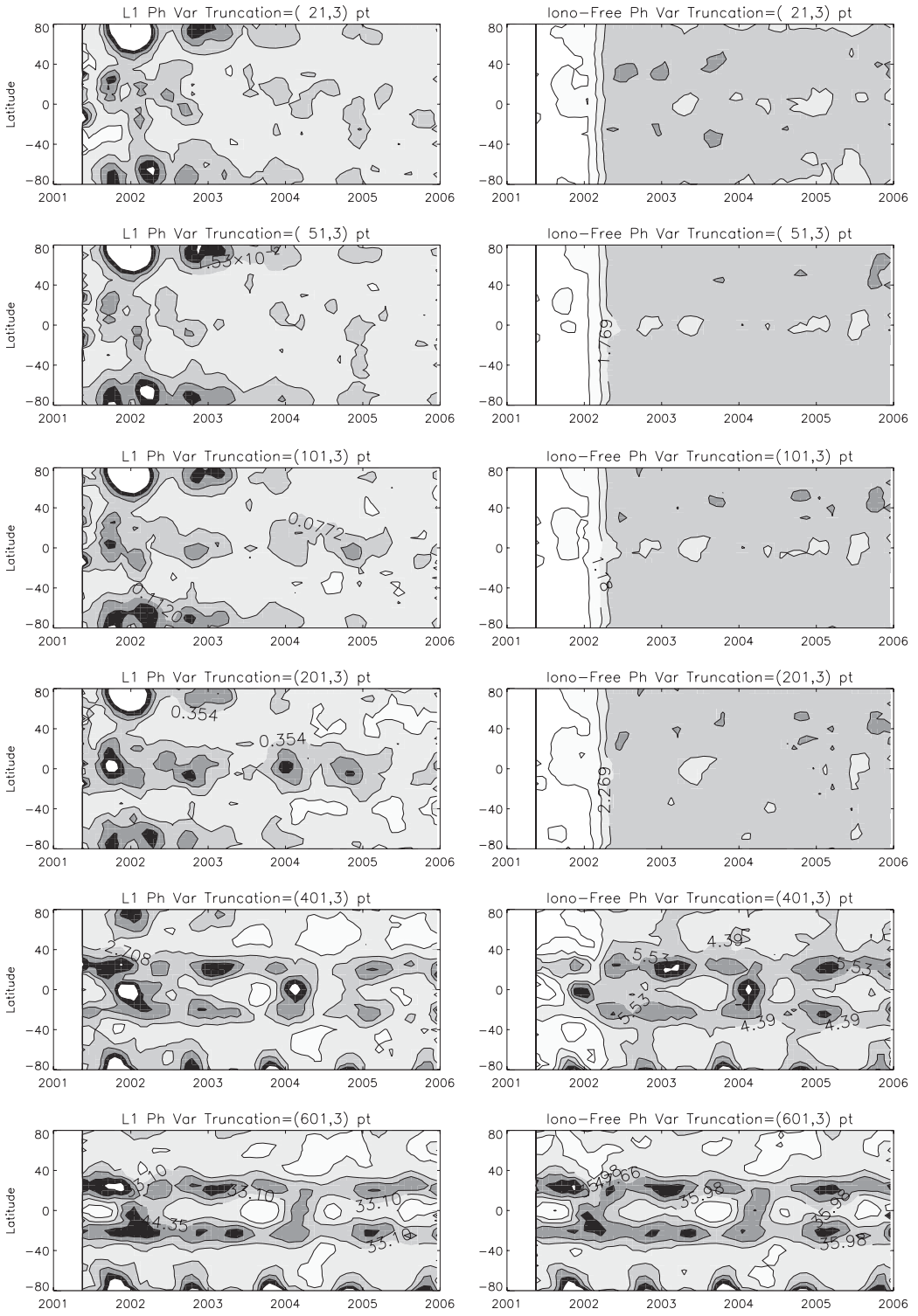

Fig. 6. Scale-dependence of the L1 and iono-free phase variances on the six band-pass filters used at the 25 km altitude. The truncation lengths of 21, 51, 101, 201, 401, and 601 points correspond to vertical scales of 0.5, 1.3, 2.5, 5, 10, and 15 km, respectively. An increase in the iono-free phase noise since February 2002 reflects operation changes. As a result of the changes, the L2 and iono-free phase measurements were significantly impacted whereas the L1 phase remains roughly same. The L1 phase variance also reveals significant seasonal variations in the tropics, likely due to the neutral atmosphere, that are beyond the sensitivity with the iono-free measurement.

inconsistent morphology, such as variations at high latitudes, indicate contaminations of ionospheric contributions. For the (401, 3) results, the variations are consistent between the L1 and iono-free measurements at most latitudes except NH high latitudes, suggesting that atmospheric variances are large enough to overcome the measurement noise and ionospheric contributions. The L1 variance for (601, 3) km is mostly neutral atmospheric variances. Spectral leaks from large-scale waves (e.g., Kelvin and Rossby GWs) to the variances can also affect the morphology as seen in Fig. 6. We investigated the variances filtered with a third-order polynomial on the phase profiles as described above and found that systematic residuals from atmospheric thermal structures with long wavelengths (e.g., QBO) are small compared to the observed atmospheric variances in Fig. 6 for 601-, 401-, and 201-point truncations. The results from the (801, 3) truncation, however, require more caution if the variance becomes $<\sim 0.3\,m^2$.

Fig. 7 shows a comparison between the CHAMP phase variance and MLS (Microwave Limb Sounder) GW variances at 10–55 km for August, September, and October 2004. The MLS was onboard NASA Aura satellite launched in July 2004, using saturated microwave limb radiances to measure GW-induced temperature fluctuations in the middle atmosphere (Wu and Waters, 1996; Wu et al., 2006). It has good sensitivity to GWs of short ($\sim$200 km) horizontal and long ($>$10 km) vertical wavelengths (Wu and Waters, 1997). The MLS GW variances should be compared to the CHAMP variances with long-wavelength cutoffs. As shown in Fig. 7, the CHAMP L1 phase variances from the (201, 3) and (401, 3) filters have better agreement with MLS monthly means at 45°S–45°N latitudes. The double peaks of MLS variances at $\sim$24 km are smeared in the CHAMP phase variances but clearly evident in the CHAMP temperature variance from a different period of time (Ratnam et al., 2004). As shown in Fig. 6, the double-peak structure correlates strongly with the QBO, reaching its maxima in early 2003 and early 2005. On the other hand, a single-peak variance, centered at the equator, has maxima in early 2002 and early 2004. The relation between these small-scale variances and the QBO is currently being investigated, and the results will be presented elsewhere.

The variances at high latitudes differ substantially between CHAMP and MLS. Such difference is coupled with ionospheric influences from the top that affect measurements at lower stratospheric tangent heights. Weak GW variances were reported for GPS/MET RO observations at high latitudes in a comparison with CRISTA (Cryogenic Infrared Spectrometers and Telescopes for the Atmosphere) temperature data in the SH (Preusse et al., 2002). The differences were explained as a missing of strong mountain waves in the GPS observations. Mountain waves in the stratosphere tend to have long vertical but short horizontal wavelengths (e.g., Fritts and Alexander, 2003). The GW sensitivity with GPS RO technique (Lange and Jacobi, 2003) is complementary to that with MLS (Wu and Waters, 1997). It should be pointed out that the CHAMP–MLS differences at high latitudes still exist when a band-pass filter (17.6 km, 5 km) is used. Thus, the differences between these observed GW climatologies are likely resulted from sensitivity differences with these observing techniques. However, to fully understand these variance differences, one needs to analyze the observational filters for CHAMP and MLS thoroughly.

In addition, further investigations are required to understand the subtropical variances near 30°N in August and September where both MLS GW variances and CHAMP E_s activity show large enhancement. The two phenomena may be connected through upward propagating GWs from deep convection, as suggested in Hocke and Tsuda (2001), which would make interpretation of the L1 phase variance more complicated at these transition altitudes. Correct interpretation requires a better understanding of the ''observational filter'' associated with these measurement techniques. The GPS RO and MLS techniques measure different parts of the GW spectra with some overlapping (Lange and Jacobi, 2003). Unless the real wave spectrum spreads over to a broad region, variance distributions observed by these instruments may not be alike each other.

4.3. Annual and QBO-like variations

In the equatorial region (2.5°S–2.5°N), the CHAMP SNR variance from the (401,3) filter exhibits a significant annual variation with downward progression in amplitude change and the coherent perturbation patterns apparently extend up to $\sim$32 km. As shown in Fig. 8, the maximum SNR/SNR_0 variance occurs in the months of northern winter at $\sim$20 km, lagging behind the maxima at $\sim$32 km by $\sim$6 months. At 20–23 km, the

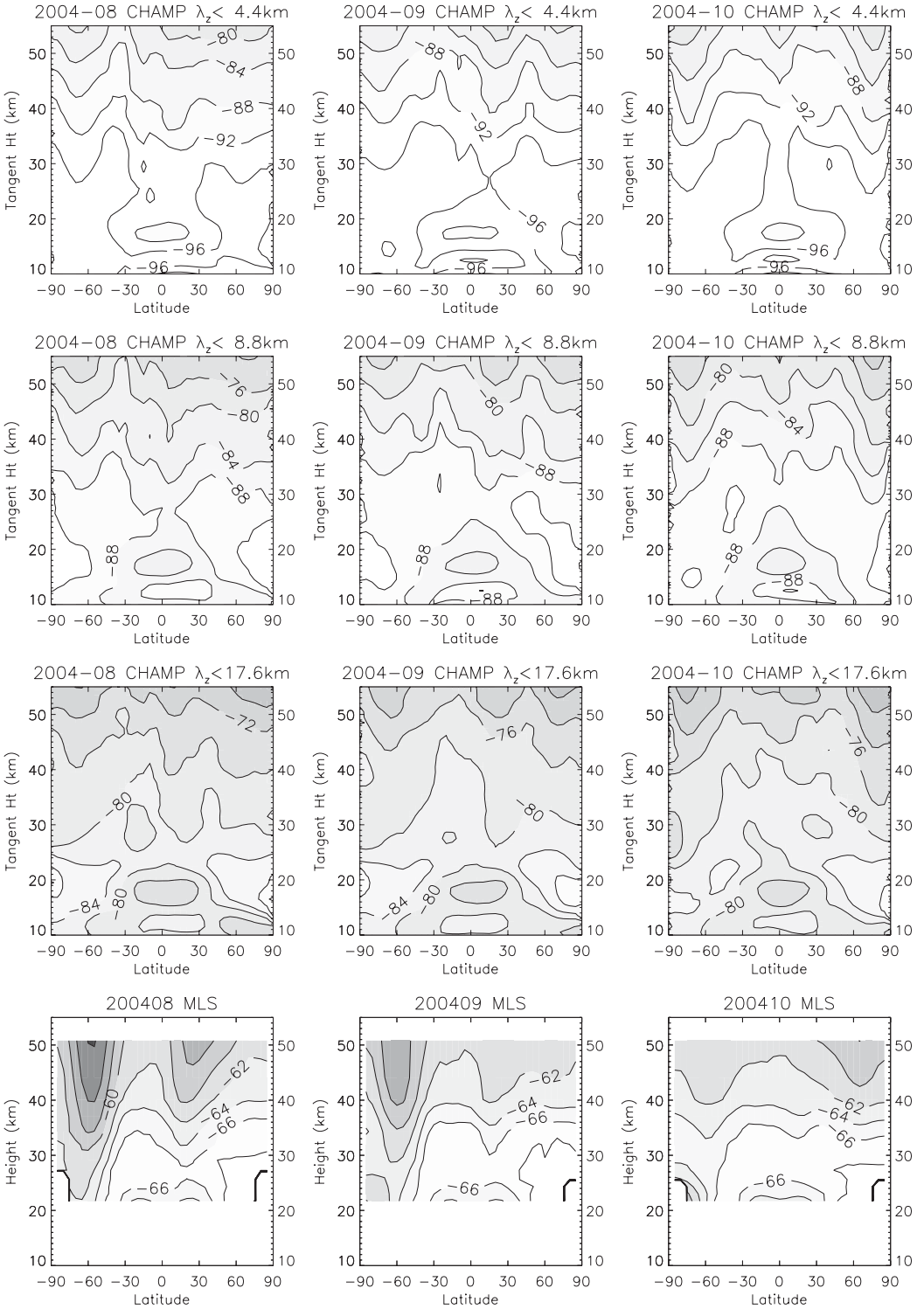

Fig. 7. Comparison of CHAMP L1 phase monthly variances with MLS for August, September, and October 2004.

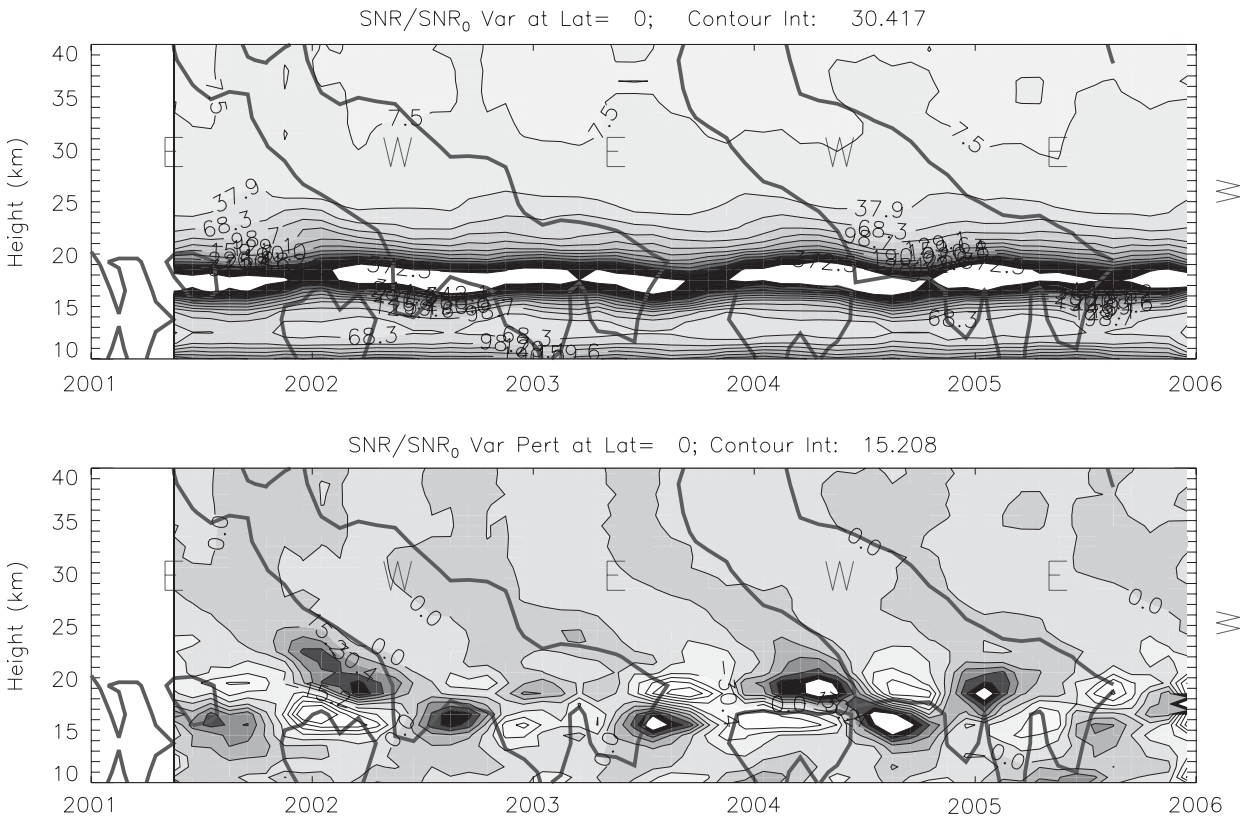

Fig. 8. Time series of the equatorial (2.5°S–2.5°N) CHAMP SNR/SNR$_0$ variance derived with the (401,3) filter (top) and deviations about its time mean (bottom). The unit is 10^{-4} and the contour interval is indicated at the top of each panel.

variance in 2003 winter is much lower than those in 2002 and 2004 but this QBO-like modulation does not extend further to higher altitudes. The SNR variances above ~32 km must be treated with caution because of likely contamination by ionospheric influences.

The L1 phase variance from the (401,3) filter produces a large QBO-like variation with smaller variances in the 2002–2003 and 2004–2005 winters compared to 2003–2004 winter (Fig. 9). The downward progress in the change of phase variance is found to be consistent with the result from the high-resolution radiosonde data (Sato and Dunkerton, 1997). The radiosonde observations showed that the GW variance of short periods (1–3 days) was weak during the westerly-to-easterly QBO phase. Possible impacts from the mean QBO temperature structures are ruled out because leak of spectral power is small if the varying backgrounds have a vertical wavelength >20 km (Schmidt et al., 2004b). However, potential impacts from the sharp tropopause structures need further investigations.

At 45°S and 45°N latitudes (Fig. 10), large annual variations are evident in the SNR variances at heights <~20 km with slightly higher extension in the northern latitude. An upward progression in the 45°N variance perturbation starts in spring at ~10 km height and ends in fall at ~20 km. At 45°S, a slight downward progression in the variance change is seen at 10–15 km heights with maxima in spring at ~15 km.

5. Discussions

The observed RO SNR and phase variances can be related qualitatively to wave properties in terms of amplitude and vertical wavelength of density fluctuations. As shown with the conceptual models outlined in the Appendices A and B, the SNR variance is proportional to wave power and inversely proportional to vertical wavelength

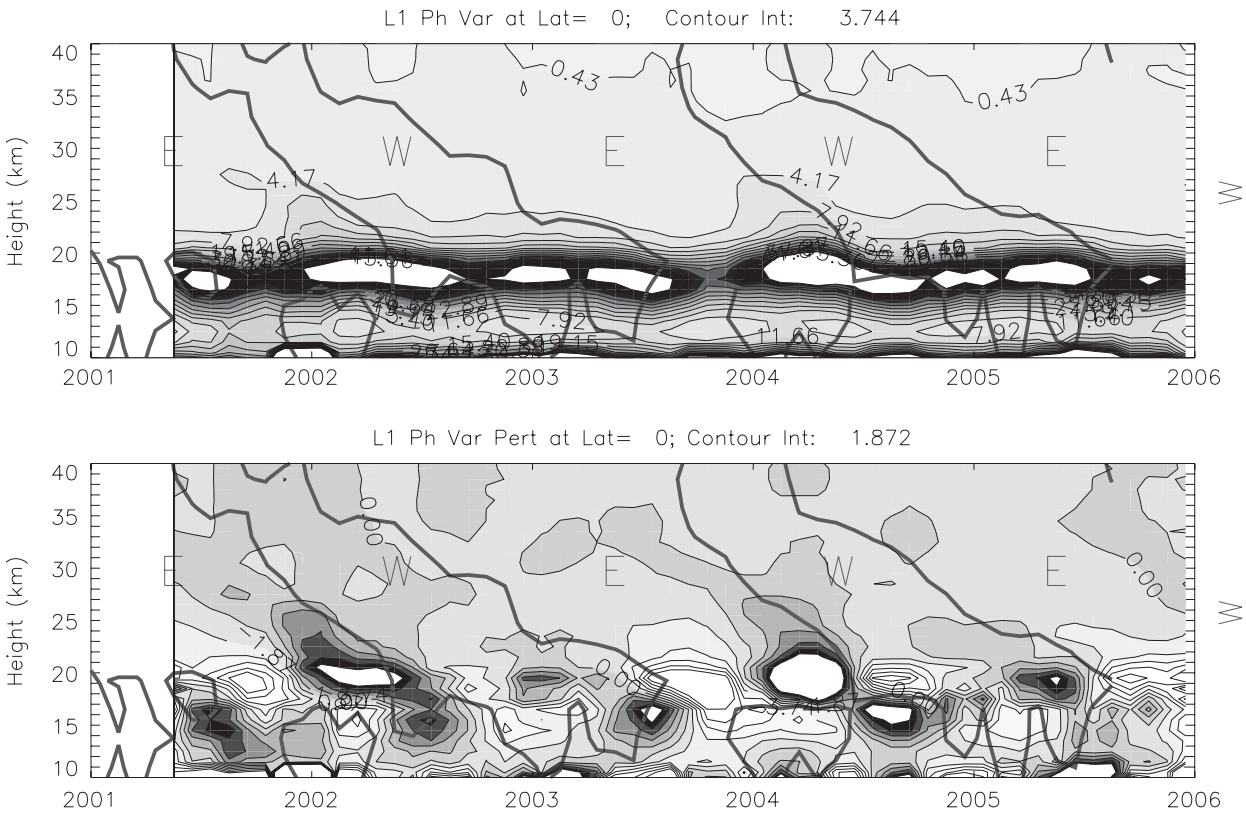

Fig. 9. Similar to Fig. 8 but for L1 phase variance at the equator. The variance and its perturbations have unit of m^2.

squared:

$$\mathrm{var}\left(\frac{\mathrm{SNR}}{\mathrm{SNR}_0}\right) \propto \left(\frac{\rho'}{\lambda_z}\right)^2 \quad \text{for the neutral atmosphere,} \tag{4A}$$

$$\mathrm{var}\left(\frac{\mathrm{SNR}}{\mathrm{SNR}_0}\right) \propto \left(\frac{\Delta\mathrm{TEC}}{\lambda_z}\right)^2 \quad \text{for the ionosphere,} \tag{4B}$$

where ρ' is the amplitude of atmospheric density perturbation due to dry air and water vapor. ΔTEC is the perturbation of total electron content along the occultation path. On the other hand, the phase variance is directly proportional to wave power without tailored by vertical wavelength. The simple analytical results are consistent to the previous finding with a more sophisticated model (Wu et al., 2005). Using a multiple phase screen (or MPS) model, Wu et al. (2005) simulated impacts of idealized E_s perturbations on the CHAMP SNR and phase variances. It was concluded that at large vertical wavelengths, the phase variance is not tapered by vertical wavelength. The variance is determined only by wave power and the truncation length used in the variance analysis.

In contrast, the SNR variance at large vertical wavelengths is determined primarily by the vertical gradient of refractivity perturbations (Karayel and Hinson, 1997), which fundamentally results in the λ_z^{-2} dependence in Eq. (4).The MPS model simulations also reveal important wave effects at small vertical wavelengths where geometric optics approximation becomes invalid. At these scales, wave interference must be taken into account for the SNR and phase calculations. Wu et al. (2005) found that the SNR and phase variances are controlled primarily by the diffraction effect of perturbing layers when the vertical wavelength becomes less than 1 km.The effect of interference tends to spread the perturbation power to a broader height (or angular) range in the observing plane, causing reduction in the SNR and phase variances. As a result, the SNR variance of E_s decreases with

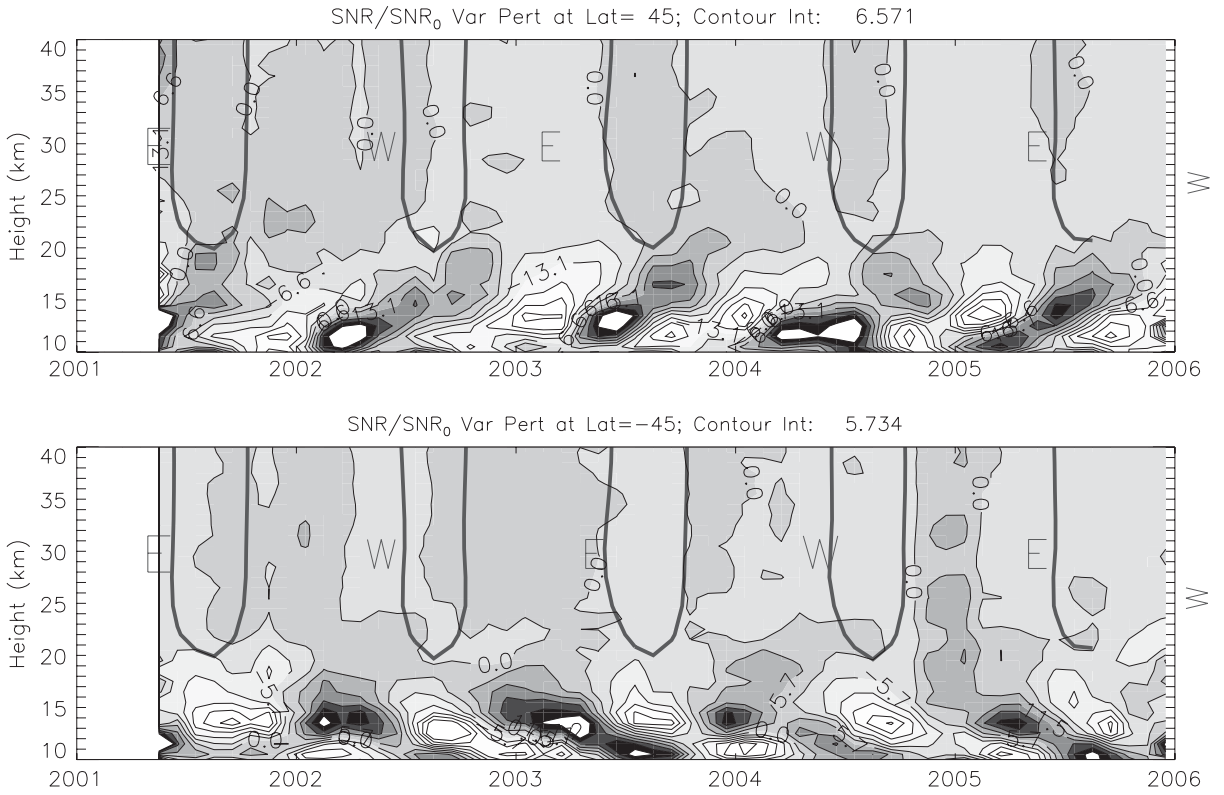

Fig. 10. Similar to the bottom panel in Fig. 8 except for SNR/SNR_0 variance perturbations at 45°S and 45°N. In the NH, the variance is dominated by an annual cycle with an upward progression in amplitude. The coherent progression is limited mostly below 20 km with a slightly high extension in the end of 2003. In the SH, the variance varies annually but lacks clear progression with height, and does not extend to the altitude as high as in the NH case.

vertical wavelength (approximately λ_z^{-2} for the same horizontal length of E_s layers). The decreasing sensitivity at both short and long ends of vertical wavelength yields peak sensitivity for the vertical wavelength of ~1.2 km.

6. Summary and future work

This paper presents preliminary work to infer small-scale fluctuations directly from RO phase and SNR data. Basic morphology and properties of small-scale SNR and phase fluctuations during 2001–2005 are investigated with band-pass filters to minimize contributions from high-frequency (>10 Hz) noise. The calculated variances are averaged into latitude and height bins on a monthly basis and studies are focused on seasonal, annual, and interannual variabilities. Several interesting features emerge from the preliminary analyses.

(1) Time series of these variances reveal strong annual and QBO-like variations in the ionosphere (due to E_s activity) and in the lower stratosphere and upper troposphere (likely due to gravity wave activity). The QBO-like modulation in the E-region implies a substantial tropical and subtropical coupling between lower and higher atmospheric dynamics, which deserves further investigations. The E_s activity peaks at ~105 km in the summer mid-latitudes and may affect the variances at tangent heights as low as 25 km. At high latitudes, the E_s variance maximizes in October–January but decreases since 2001 as a result of the 11-year solar cycle.

(2) The tropical variances in the lower stratosphere correlate well with tropopause height variations. High tropopause occurs during January–February, corresponding to the large SNR and phase variances at 18.5 km. In summer, tropical tropopause is generally lower with the variance peak near ~16 km. Both the SNR and phase variances exhibit a QBO-like variation with downward progression in the variance amplitude. The coherent

downward progression can be observed from 15 to ~30 km, suggesting strong interactions between small-scale variances and the QBO phenomenon. At 25 km, the latitudinal distribution of the L1 variance alternates between single-peak and double-peak structures with a QBO-like period, which will be studied in further detail.

A conceptual model is used to better understand the observed SNR and phase variances. For exponential and layered refractivity profiles, the SNR variances are proportional to wave power but inversely proportional to vertical wavelength. The phase variances are simply proportional to wave power without being scaled by vertical wavelength. This conceptual model neglects potential effects of horizontal wave structures, which sometimes can be important as well. The instrument "observational filter", critical to understand gravity wave variances measured by different techniques (Alexander, 1998; Wu et al., 2006), is not well defined and requires more quantitative evaluation.

The L1 phase variance shows that it contains useful information on small-scale variability at heights >30 km. The iono-free phase variance would be the best measurement for studying neutral atmospheric variabilities at higher altitudes if the L2 measurement noise can be reduced. At the current L2 noise level, the iono-free phase measurement is only useful up to ~30 km. Since E_s normally creates fluctuations of high (>1 Hz) frequencies, the 1-s (or 50-point) smoothing in the Level 2 retrieval is an efficient way for removing this ionospheric contribution.

The variance method used in this study can be also applied to ground-based GPS measurements. Since E_s layers often have embedded field-aligned fine structures (Fukao et al., 1998), one may bin the ground-based SNR and phase variances according to the dip angle and strength of the geomagnetic field to quantify variations of GPS receiver scintillation. The signal with link in parallel to the geomagnetic field should have larger values than received from other directions. For the ground-based tropospheric delays, organized short-scale weather system would produce larger variances in preferred directions.

Acknowledgments

This research was performed at the Jet Propulsion Laboratory, California Institute of Technology, under contract with the National Aeronautics and Space Administration (NASA). The author would like to thank UK Met Office for providing the assimilated wind dataset and two anonymous reviewers for valuable suggestions and comments.

Appendix A. Atmospheric SNR and phase perturbations

In geometric optics approximation, the bending angle of radio waves through a spherically symmetric atmosphere can be related to the index of refraction as

$$\alpha(a) = -\int_a^\infty \frac{2a}{n\sqrt{n^2r^2 - a^2}} \frac{\mathrm{d}n}{\mathrm{d}r}\,\mathrm{d}r, \tag{A.1}$$

where $\alpha(a)$ is the bending angle at tangent height and r is radius (Born and Wolf, 1980). The refractive index n is usually expressed in terms of refractivity N:

$$n = 1 + N \times 10^{-6} \tag{A.2}$$

and

$$N = a_{\mathrm{dry}}\rho_{\mathrm{d}} + a_{\mathrm{wv}}\frac{\rho_{\mathrm{wv}}}{T} + a_{\mathrm{e}}\frac{n_{\mathrm{e}}}{f^2} + a_{\mathrm{water}}W_{\mathrm{w}} + a_{\mathrm{ice}}W_{\mathrm{i}} + \mathrm{O}\left(\frac{1}{f^3}\right), \tag{A.3}$$

where air and water vapor density ρ_{d} and ρ_{wv} are in $\mathrm{kg/m^3}$. Air temperature T, electron number density n_{e}, and radio wave frequency f have units of K, $\mathrm{m^{-3}}$, and MHz, respectively. W_{w} and W_{i} are liquid and ice water contents in $\mathrm{g/m^3}$. The corresponding coefficients are given by

$$a_{\mathrm{dry}} = 222.7\,\mathrm{m^3\,kg^{-1}}$$
$$a_{\mathrm{wv}} = 1.07 \times 10^6\,\mathrm{m^3\,kg^{-1}}$$
$$a_{\mathrm{e}} = -4.03 \times 10^7\,\mathrm{m^3\,MHz^2}$$
$$a_{\mathrm{water}} = 1.4\,\mathrm{m^3\,g^{-1}}$$
$$a_{\mathrm{ice}} = 0.6\,\mathrm{m^3\,g^{-1}}.$$

Since $n \sim 1$, Eq. (A.1) can be approximately written as

$$\alpha(a) \approx -\int_a^\infty \frac{2 \times 10^{-6} a}{\sqrt{r^2 - a^2}} \frac{\mathrm{d}N}{\mathrm{d}r}\,\mathrm{d}r. \tag{A.4}$$

For the neutral atmosphere, let us consider simple exponential height dependence for N as due to air and water vapor density variations. In particular, we assume $N(r) = N_a \mathrm{e}^{-(r-a)/H}$ for an atmosphere without perturbations, where scale height H is

constant and N_a is the value of N at $r = a$. Then, Eq. (A.4) can be rewritten as

$$\alpha(a) = \int_a^\infty \frac{2\times10^{-6}a}{\sqrt{r^2-a^2}}\frac{N_a}{H}\,\mathrm{e}^{-(r-a/H)}\,\mathrm{d}r. \tag{A.5}$$

Reorganizing Eq. (A.5), we have

$$\begin{aligned}\alpha(a) &= \int_1^\infty \frac{2\times10^{-6}}{\sqrt{x^2-1}}\frac{N_a a}{H}\,\mathrm{e}^{-(a/H)(x-1)}\,\mathrm{d}r \\ &= \frac{2\times10^{-6}N_a a}{H}\int_0^\infty \frac{\mathrm{e}^{-(a/H)t}}{\sqrt{(2+t)t}}\,\mathrm{d}t.\end{aligned} \tag{A.6}$$

For $a/H \gg 1$, which holds for RO, we have

$$\sqrt{(2+t)t} \approx \sqrt{2t}. \tag{A.7}$$

Substituting Eq. (A.7) into Eq. (A.6), we have the integral in terms of a gamma function:

$$\begin{aligned}\alpha(a) &= \frac{2\times10^{-6}N_a a}{H}\,\Gamma(1/2)\sqrt{\frac{H}{2a}} \\ &= 2.51\times10^{-6}N_a\sqrt{\frac{a}{H}}.\end{aligned} \tag{A.8}$$

For small perturbations of vertical wavelength λ_z near tangent height a, say, $N_a = \overline{N}_a + N'(\lambda_z)\cos(2\pi a/\lambda_z)$, we have

$$\alpha(a) = \bar{\alpha}(a) + \alpha'(\lambda_z, a)\cos(2\pi a/\lambda_z), \tag{A.9}$$

where the wave amplitude $N'(\lambda_z)$ can be a function of wavelength.

A.1. Phase perturbations

The excessive phase delay and the bending angle are related by

$$\phi = a\alpha. \tag{A.10}$$

Thus, the phase perturbation can be expressed as

$$\phi = \bar{\phi} + \phi'(\lambda_z)\cos[2\pi a/\lambda_z]$$

$$\text{or}\quad \mathrm{var}\left(\frac{\phi'}{\bar{\phi}}\right) \propto N'^2. \tag{A.11}$$

Thus, the variance of phase perturbations is directly proportional to the wave amplitude squared. Since N' may increase with wavelength, the variances from different high-pass filters will yield different results depending on vertical wavenumber spectra.

A.2. SNR perturbations

The intensity of RO signal is related to the vertical gradient of bending angle with respect to tangent height, known as the focusing/defocusing effect. If the distances from tangent point to receiver (D_r) and to transmitter (D_t) are known, the intensity change can be determined by (e.g., Hajj et al., 2002)

$$\frac{I}{I_0} = \left(\frac{\mathrm{SNR}}{\mathrm{SNR}_0}\right)^2 = \left\{1 - \frac{\mathrm{d}\alpha}{\mathrm{d}a}\frac{D_\mathrm{r}D_\mathrm{t}}{D_\mathrm{r}+D_\mathrm{t}}\right\}^{-1}. \tag{A.12}$$

From Eq. (A.9), if $\overline{N}_a = N_0\mathrm{e}^{-(a-R_\mathrm{e}/H)}$, we have

$$\frac{\mathrm{d}\bar{\alpha}}{\mathrm{d}a} = 2.51\times10^{-6}N_a\left(\frac{1}{2\sqrt{aH}} - \sqrt{\frac{a}{H^3}}\right). \tag{A.13}$$

For typical Earth's atmospheric applications, $a\sim6400$ km and $H\sim7$ km; the first term in Eq. (A.13) can be neglected and Eq. (A.13) is reduced to

$$\frac{\mathrm{d}\bar{\alpha}}{\mathrm{d}a} \approx -2.51\times10^{-6}N_a\sqrt{\frac{a}{H^3}}. \tag{A.14}$$

For the perturbations, we have

$$\begin{aligned}\frac{\mathrm{d}\alpha'}{\mathrm{d}a} &= 2.51\times10^{-6}N' \\ &\times\left\{\frac{1}{2\sqrt{aH}}\cos\left(\frac{2\pi a}{\lambda_z}\right) - \sqrt{\frac{a}{H}}\frac{2\pi}{\lambda_z}\sin\left(\frac{2\pi a}{\lambda_z}\right)\right\}.\end{aligned} \tag{A.15}$$

Normally, we are interested in 1–20 km vertical wavelengths, which makes the first term in Eq. (A.15) negligible. Thus, combining Eqs. (A.14)

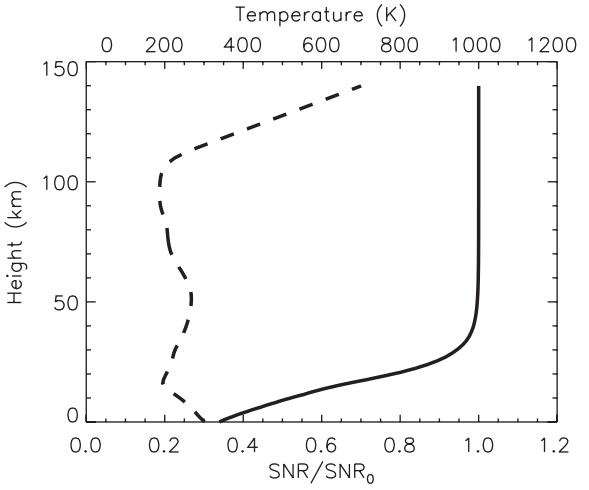

Fig. A1. Normalized SNR profile for typical GPS/CHAMP occultation parameters. From the transmitter and receiver distances, D_0 is ~2800 km. This profile assumes a scale height of 7 km and a temperature profile (dashed line).

and (A.15) yields

$$\frac{\mathrm{d}\alpha'}{\mathrm{d}a} = -2.51\times10^{-6}\sqrt{\frac{a}{H}}\left\{\frac{N_a}{H}+\frac{2\pi}{\lambda_z}N'\sin\left(\frac{2\pi a}{\lambda_z}\right)\right\}. \tag{A.16}$$

Substituting Eq. (A.16) into Eq. (A.12), we obtain

$$\frac{I}{I_0}\approx\left\{1+2.51\times10^{-6}D_0\sqrt{\frac{a}{H}}\left[\frac{N_a}{H}+\frac{2\pi N'}{\lambda_z}\sin\left(\frac{2\pi a}{\lambda_z}\right)\right]\right\}^{-1}, \tag{A.17}$$

where $D_0 \equiv D_\mathrm{r}D_\mathrm{t}/D_\mathrm{r}+D_\mathrm{t}$. In the case of no perturbations, i.e., $N'=0$, Eq. (A.17) becomes

$$\frac{\overline{\mathrm{SNR}}}{\mathrm{SNR}_0}\approx\left\{1+2.51\times10^{-6}N_a\sqrt{\frac{a}{H^3}}D_0\right\}^{-1/2}. \tag{A.18}$$

As shown in Fig. A1, the SNR decreases gradually with tangent height below ~30 km as N_a in Eq. (A.18) increases exponentially with decreasing height. Eq. (A.18) also shows strong dependence of SNR amplitude on scale height. As the scale height increases/decreases, it could produce strong focusing/defocusing effects on the receiver power such that the signal may be lost temporarily.

For small-amplitude perturbations, the variance of SNR over its local mean can be approximated by

$$\mathrm{var}\left(\frac{\mathrm{SNR}}{\overline{\mathrm{SNR}}}\right)\approx\frac{\pi^2 a}{2H}\left\{\frac{\pi N' D_0}{\lambda_z\left[1+2.51\times10^{-6}N_a\sqrt{a/H^3}D_0\right]}\right\}^2$$

$$\text{or}\quad var\left(\frac{\mathrm{SNR}}{\overline{\mathrm{SNR}}}\right)\propto\left(\frac{N'}{\lambda_z}\right)^2. \tag{A.19}$$

As indicated by Eq. (A.19), the variance of normalized SNR is proportional to the squared amplitude of density fluctuations and reversely proportional to the vertical wavelength squared. In other words, waves of long vertical wavelengths do not contribute the SNR variance efficiently.

Appendix B. Ionospheric SNR and phase perturbations

For the ionospheric perturbations, let us consider simple cases where electrons form layered structures such as sporadic-E. Hence, the phase delay ϕ can be written as

$$\phi = N(a)L = a_\mathrm{e}\frac{h\mathrm{TEC}}{f^2}, \tag{B.1}$$

where $h\mathrm{TEC}\equiv n_\mathrm{e}(a)L$ is the total horizontal electron content along occultation path, L is length of electron layer, a is tangent height, and a_e and n_e are defined in Eq. (A.3). Therefore, small-scale perturbations in $n_\mathrm{e}(r)$ or L can induce phase oscillations proportionally, say,

$$\phi = \overline{\phi}+\phi'\cos\left(\frac{2\pi a}{\lambda_z}\right) \tag{B.2}$$

and

$$\mathrm{var}(\phi)\propto\phi'^2. \tag{B.3}$$

To obtain the SNR perturbations, we need to first find the derivative of bending angle with respect to height. From Eqs. (A.10) and (B.2), we have

$$\frac{\mathrm{d}\alpha}{\mathrm{d}a} = -\frac{1}{a}\left\{\frac{\phi}{a}+\frac{\phi'}{\lambda_z}\sin\left(\frac{2\pi a}{\lambda_z}\right)\right\}$$

$$= -\overline{\frac{\mathrm{d}\alpha}{\mathrm{d}a}}-\frac{\phi'}{a}\left\{\frac{1}{a}+\frac{1}{\lambda_z}\sin\left(\frac{2\pi a}{\lambda_z}\right)\right\}, \tag{B.4}$$

where $\overline{\mathrm{d}\alpha}/\mathrm{d}a\equiv\bar{\phi}/a^2$. Since we are only interested in the cases where $\lambda_z \ll a$, the first perturbation term in Eq. (B.4) can be neglected. For small-amplitude perturbations, we can express the SNR variance as

$$\mathrm{var}\left(\frac{\mathrm{SNR}}{\mathrm{SNR}_0}\right)\approx\frac{\pi}{8}\left(\frac{\phi D_0}{a\lambda_z}\right)^2\left\{1+\frac{\overline{\phi}D_0}{a^2}\right\}^{-3} \tag{B.5}$$

or

$$\mathrm{var}\left(\frac{\mathrm{SNR}}{\mathrm{SNR}_0}\right)\propto\left(\frac{\phi'}{\lambda_z}\right)^2. \tag{B.6}$$

This is similar to Eq. (A.19) where the SNR variance is proportional to the squared amplitude of perturbations but inversely to the vertical wavelength squared.

References

Alexander, M.J., 1998. Interpretations of observed climatological patterns in stratospheric gravity wave variance. Journal of Geophysical Research 103, 8627–8640.

Born, M., Wolf, E., 1980. Principles of Optics, sixth ed. Pergamon, Tarrytown, New York.

Fritts, D.C., Alexander, M.J., 2003. Gravity wave dynamics and effects in the middle atmosphere. Reviews of Geophysics 41 (1), 1003.

Fukao, S., Yamamoto, M., Tsunoda, R.T., Hayakawa, H., Mukai, T., 1998. The SEEK (sporadic-E experiment over Kyushu) campaign. Geophysical Research Letters 25 (11), 1761–1764.

Gavrilov, N.M., Karpova, N.V., Jacobi, Ch., Gavrilov, A.N., 2004. Morphology of atmospheric refraction index variations at different altitudes from GPS/MET satellite observations.

Journal of Atmospheric and Solar-Terrestrial Physics 66, 427–435.
Hajj, G.A., Romans, L.J., 1998. Ionospheric electron density profiles obtained with the Global Positioning System: results from the GPS/MET experiment. Radio Science 33, 175–190.
Hajj, G.A., et al., 2002. A technical description of atmospheric sounding by GPS occultation. Journal of Atmospheric and Solar-Terrestrial Physics 64, 451–469.
Hajj, G.A., et al., 2004. CHAMP and SAC-C atmospheric occultation results and intercomparisons. Journal of Geophysical Research 109 (D6), D06109.
Hocke, K., Tsuda, T., 2001. Gravity waves and ionospheric irregularities over tropical convection zones observed by GPS/MET radio occultation. Geophysical Research Letters 28 (14), 2815–2818.
Hocke, et al., 2001. Global sounding of sporadic E layers by the GPS/MET radio occultation experiment. Journal of Atmospheric and Solar-Terrestrial Physics 63, 1973–1980.
Igarashi, K., Pavelyev, A., Wickert, J., et al., 2002. Application of radio holographic method for observation of altitude variations of the electron density in the mesosphere/lower thermosphere using GPS/MET radio occultation data. Journal of Atmospheric and Solar-Terrestrial Physics 64 (8–11), 959–969.
Karayel, E.T., Hinson, D.P., 1997. Sub-Fresnel-scale vertical resolution in atmospheric profiles from radio occultation. Radio Science 32, 411–423.
Kursinski, et al., 1997. Observing Earth's atmosphere with radio occultation measurements using the Global Positioning System. Journal of Geophysical Physics 102 (D19), 23429–23465.
Lange, M., Jacobi, Ch., 2003. Analysis of gravity waves from radio occultation measurements. In: Reigber, Ch., Lühr, H., Schwintzer, P. (Eds.), First CHAMP Mission Results for Gravity, Magnetic and Atmospheric Studies. Springer, Berlin, pp. 479–484.
Liou, Y.A., Pavelyev, A.G., Wickert, J., 2005. Observation of the gravity waves from GPS/MET radio occultation data. Journal of Atmospheric and Terrestrial Physics 67, 219–228.
Maksyutin, S.V., Sherstyukov, O.N., Fahrutdinova, A.N., 2001. Dependence of sporadic-E layer and lower thermosphere dynamics on solar activity. Advances in Space Research 27, 1265–1270.
Marquardt, C., Healy, S.B., 2005. Measurement noise and stratospheric gravity wave characteristics obtained from GPS Occultation Data. Journal of the Meteorological Society of Japan 83 (3), 417–428.
Mathews, J.D., 1998. Sporadic E: current views and recent progress. Journal of Atmospheric and Terrestrial Physics 60, 413–435.
Pavelyev, A., Tsuda, T., Igarashi, K., Liou, Y.A., Hocke, K., 2003. Wave structures in the electron density profile in the ionospheric D- and E-layers observed by radio holography analysis of the GPS/MET radio occultation data. Journal of Atmospheric and Solar-Terrestrial Physics 65, 59–70.
Preusse, P., et al., 2002. Space-based measurements of stratospheric mountain waves by CRISTA—1. Sensitivity, analysis method, and a case study. Journal of Geophysical Research-Atomospheres 107 (D23), 8178.
Randel, W.J., Wu, F., 2005. Kelvin wave variability near the equatorial tropopause observed in GPS radio occultation measurements. Journal of Geophysical Research 110, D03102.
Ratnam, M.V., Tetzlaff, G., Jacobi, C., 2004. Global and seasonal variations of stratospheric gravity wave activity deduced from the *CHAMP*/GPS satellite. Journal of the Atmospheric Sciences 61, 1610–1620.
Reid, G., Gage, K., 1981. On the annual variation of height of the tropical tropopause. Journal of the Atmospheric Sciences 38, 1928–1937.
Reigber, Ch., Luhr, H., Schwintzer, P., 2002. CHAMP mission status. Advances in Space Research 30 (2), 129–134.
Salby, M., Callaghan, P., 2004. Control of the tropical tropopause and vertical transport across it. Journal of Climate 17, 966.
Sato, K., Dunkerton, T.J., 1997. Estiamtes of momentum flux associated with equatorial Kelvin and gravity waves. Journal of Geophysical Research 102, 26,247–26,261.
Schmidt, T., Wickert, J., Beyerle, G., Reigber, C., 2004a. Tropical tropopause parameters derived from GPS radio occultation measurements with CHAMP. Journal of Geophysical Research 109, D13105.
Schmidt, T., Heise, S., Wickert, J., Beyerle, G., Reigber, C., 2004b. GPS radio occultation with CHAMP: monitoring of climate change parameters. Atmospheric Chemistry and Physics Discussion 4, 7837–7857.
Spilker, J.J., 1980. GPS Signal Structure and Performance Characteristics. Global Positioning System, Institute of Navigation, Washington, DC, pp. 29–54.
Straus, P.R., Anderson, P.C., Danaher, J.E., 2003. GPS occultation sensor observations of ionospheric scintillation. Geophysical Research Letters 30 (8) (Art. no. 1436).
Tsuda, T., Nishida, M., Rocken, C., Ware, R.H., 2000. A global morphology of gravity wave activity in the stratosphere revealed by the GPS occultation data (GPS/MET). Journal of Geophysical Research 105, 7257–7273.
Ware, R., et al., 1996. GPS sounding of the atmosphere from low Earth orbit: preliminary results. Bulletin of the American Meteorological Society 77, 19–40.
Whitehead, J.D., 1989. Recent work on mid-latitude and equatorial sporadic E. Journal of Atmospheric and Terrestrial Physics 51, 401–424.
Wickert, J., et al., 2001. Atmosphere sounding by GPS ratio occultation: first results from CHAMP. Geophysical Research Letters 28, 3263–3266.
Wickert, J.A., et al., 2004. Amplitude scintillations in GPS signals as a possible indicator of ionospheric structures. Geophysical Research Letters 31 (24), L24801 (1-4).
Wu, D.L., Waters, J.W., 1996. Satellite observations of atmospheric variances: a possible indication of gravity waves. Geophysical Research Letters 23, 3631–3634.
Wu, D.L., Waters, J.W., 1997. Observations of gravity waves with the UARS Microwave Limb Sounder. In: Hamilton, K. (Ed.), Gravity Wave Processes and Their Parameterization in Global Climate Models, NATO ASI Series, vol. 50. Springer, Berlin, New York, p. 404.
Wu, D.L., Ao, C.O., Hajj, G.A., de la Torre Juarez, M., Mannucci, A.J., 2005. Sporadic-E Morphology from GPS-CHAMP Radio Occultation. Journal of Geophysical Review-Space 110 (A1) Art. No. A01306.
Wu, D.L., et al., 2006. Remote sounding of atmospheric gravity waves with satellite limb and nadir techniques. Advances in Space Research, in press.
Yeh, K.C., Liu, C.H., 1982. Radio wave scintillations in the ionosphere. Proceedings of the IEEE 70 (4), 324–360.